

Electronic structure of a nodal line semimetal candidate TbSbTe

Iftakhar Bin Elius¹, Jacob F Casey², Sabin Regmi^{1,3}, Volodymyr Buturlim⁴,
Anup Pradhan Sakhya¹, Milo Sprague¹, Mazharul Islam Mondal¹, Nathan Valadez¹,
Arun K Kumay¹, Justin Scrivens¹, Yenugonda Venkateswara², Shovan Dan⁵
Tetiana Romanova⁵, Arjun K Pathak², Krzysztof Gofryk³, Andrzej Ptok⁶,
Dariusz Kaczorowski⁵, Madhab Neupane^{*1}

¹*Department of Physics, University of Central Florida, Orlando, Florida 32816, USA*

²*Department of Physics, SUNY Buffalo State, Buffalo, New York 14222, USA*

³*Center for Quantum Actinide Science and Technology, Idaho National Laboratory, Idaho Falls, Idaho 83415, USA*

⁴*Glenn T. Seaborg Institute, Idaho National Laboratory, Idaho Falls, Idaho 83415, USA*

⁵*Institute of Low Temperature and Structure Research,
Polish Academy of Sciences, Okólna 2, PL-50-422 Wrocław, Poland*

⁶*Institute of Nuclear Physics, Polish Academy of Sciences,
W. E. Radzikowskiego 152, PL-31342 Kraków, Poland*

*Corresponding author: madhab.neupane@ucf.edu

Abstract

The $LnSbTe$ ($Ln = \text{Lanthanides}$) family, like isostructural $ZrSiS$ -type compounds, has emerged as a fertile playground for exploring the interaction of electronic correlations and magnetic ordering with the nodal line band topology. Here, we report a detailed electronic band structure investigation of $TbSbTe$, corroborated by electrical transport, thermodynamic, and magnetic studies. Temperature-dependent magnetic susceptibility and thermodynamic transport studies indicate the onset of antiferromagnetic ordering below $T_N \sim 5.1$ K. The electronic band structure study, carried out with high-resolution angle-resolved photoemission spectroscopy (ARPES) measurements aided with density functional theory based first-principles calculations reveals presence of nodal lines in the $\Gamma - X$ high symmetry direction, forming a diamond-shaped nodal plane around Γ high symmetry point. A strongly photon energy dependent nodal feature located at the X point of the surface Brillouin zone, indicating an extended nodal line along $X - R$ direction, is also observed. This study elucidates the intricate interplay among symmetry-protected band characteristics, the influence of spin-orbit coupling, magnetism, and topological properties.

I. INTRODUCTION

Since the discovery of topological insulators (TIs), the fascinating field of topological quantum materials (TQMs) has emerged as a new frontier of physics [1–4]. Serving as the arena for numerous foundational physical phenomena, these topological materials are continually evolving through robust theoretical and experimental investigations. This evolution has fostered the recognition of a variety of topological semimetals, including but not limited to Dirac [5–8] and Weyl semimetals [9–13], nodal line semimetals (NLSMs) [14–22], and Dirac nodal arcs [23, 24]. In a system with both time-reversal symmetry and inversion symmetry, band crossings can lead to the formation of Dirac nodes. At a Dirac node, two doubly degenerate bands touch each other, resulting in a four-fold degenerate crossing point. The linear dispersion relation around the Dirac node leads to massless Dirac fermions as the low-energy excitations in the system. One can classify or differentiate these TQMs based on the dimensionality of their band interactions or crossings in the momentum space [5, 7]. The idea of zero dimensional band contact points in Dirac or Weyl semimetals is further extended to higher dimensional nodal lines or surfaces [14, 16, 25]. In NLSMs, the band interactions extend in forms of lines or closed loops, which are protected by extra

symmetries like mirror reflection, inversion, time-reversal, spin-rotation or nonsymmorphic symmetries [14, 16, 17, 26]. Nonsymmorphic symmetry incorporates a point group operation like fractional lattice translation with a nonprimitive lattice translation like screw axis or glide operation [27]. The pursuit of nonsymmorphic topological materials has been largely navigated by the seminal research throughout last few years, yet the number of material families featuring non-accidental nodal lines bereft of spin orbit coupling (SOC) is significantly limited [17, 28–30]. Some of the recent studies elucidated the possibility of continuous Dirac nodal points, under the condition that 2D square motifs twisted into hosting unit cell leading to a glide symmetry [28, 29].

These theoretical speculations came into existence since such nodal line topological phases were observed in ZrSiS followed by other MZX (M = Transition elements, Z = Si, Ge, Sb, Sn and X = S, Se, Te) materials with PbFCl type crystal structure [16, 17]. When the transition metals are replaced by rare earth elements, different topological properties can be expected due to the correlations between $4f$ and conduction band electrons and magnetism inherent to $4f$ states within the $LnSbTe$ (Ln =lanthanides) family. GdSbTe, one of the first materials reported from this family, has ZrSiS like nodal line characteristics, translated in energy positions [31]. In HoSbTe, SOC gap opening was experimentally observed at X point [32, 33], turning it into a promising material for weak topological insulator. Also its band structure has been reported to show magnetism driven changes upon antiferromagnetic (AFM) to ferromagnetic (FM) transition near 4 K [33]. Similar metamagnetic transitions [34], charge density wave (CDW) state and weak Kondo effect, were observed in CeSbTe [34–36]. In LaSbTe, at least two nodal lines along $R-X$ and $A-M$ directions were found to be robust against SOC protected by the nonsymmorphic symmetry [37]. Angle resolved photoemission spectroscopy (ARPES) studies on NdSbTe revealed two nodal lines along $R-X$ and one diamond shaped nodal line structure around the Γ point, as well as bands forming nodal lines along $\Gamma-M$ direction [38]. Magnetic and electronic study on NdSbTe revealed characteristic metamagnetic transitions in AFM region (below $T_N \sim 2.7$ K), Kondo localization and enhanced electronic correlation [39]. Experimental studies on SmSbTe showed multiple Dirac nodes which are part of nodal lines along $\Gamma-X$ and $X-R$ high symmetry (HS) directions [40, 41]. Very recently, ARPES based studies on PrSbTe revealed similar electronic structure with gapless nodal line features [42]. The Terbium variant of this series, TbSbTe remains underexplored with respect to the employment

of experimental methodologies for the simultaneous investigation of its electronic structure and its electrical, magnetic, and thermodynamic properties. A preceding analysis utilizing neutron diffraction methods on TbSbTe brought to light the existence of competing magnetic phases within the AFM state [43]. Complementary to this, another study on TbSbTe presented an amalgamation of thermodynamic, magnetic, and electronic transport measurements, supplemented by theoretical computations of the electronic band structure [44]. Notwithstanding these contributions, an experimental exploration of TbSbTe’s electronic band structure via ARPES with comprehensive integration with thermodynamic, electronic and magnetic measurements, to scrutinize the nodal line attributes of this variant remains unreported. This advancement is poised to significantly enrich our understanding of the unique quantum properties of this lesser-studied compound.

In this paper, we present thermodynamic, magnetic, electrical transport and magnetoresistive studies of the TbSbTe single crystals. To investigate the electronic band structure of the material, we performed our electronic band structure studies on TbSbTe via ARPES, corroborated with the first principles calculations. The ARPES measurements were carried out at paramagnetic (PM) phase (at 18 K), that harbor persistent nodal line like features along several HS directions. Within the resolution of the ARPES spectra, we observe gapless band crossings along the $\bar{\Gamma} - \bar{X}$ and $\bar{\Gamma} - \bar{M}$ directions that form a nodal line along bulk X-R line and a diamond shape centered at the $\bar{\Gamma}$ point in $k_x - k_y$ plane, respectively. This research provides key insights into the electronic structure and topological states of TbSbTe, introducing a valuable foundation for understanding the topological properties of $LnSbTe$ family.

II. METHODS

Crystal synthesis and characterization

High quality single crystals of TbSbTe were grown using the self-flux method. The reactants were mixed in a stoichiometric composition and placed in an alumina crucible and then sealed in a quartz ampule in vacuum. The ampule was then placed in a muffle furnace and heated to $1000^\circ C$ at a rate of $10^\circ C/h$. The temperature was held there for 10 h and then cooled to $600^\circ C$ at a rate of $2^\circ C/h$, then excess Sb flux was separated using a centrifuge followed by a natural cooling of the sample.

The chemical composition and phase purity of the crystals were ascertained through energy-dispersive X-ray (EDX) analysis, conducted using a FEI scanning electron microscope outfitted with an EDAX Genesis XM4 spectrometer. Furthermore, the crystal structure was validated by powder X-ray diffraction (XRD) analysis, performed on finely ground polycrystals of TbSbTe using a PANalytical X’pert Pro diffractometer equipped with $Cu - K_{\alpha}$ radiation. The orientation of the crystals selected for physical properties measurements was determined by means of back-scattered Laue diffraction, carried out on a Proto Manufacturing Laue-COS camera.

Thermodynamic and electrical transport measurements

Magnetic measurements were carried out in the temperature interval 2-300 K in magnetic fields up to 14 T using a Quantum Design DynaCool-14 Physical Property Measurement System (PPMS). magnetic field. The heat capacity was measured from 1.72 to 210 K employing relaxation technique and two- τ model implemented in the PPMS platform.

Electrical transport measurements were performed in a thin bar-shaped piece of crystal (cross section: $244.4 \times 155.5 \mu\text{m}^2$, and distance between voltage probe: $644.4 \mu\text{m}$) using a commercial PPMS platform. The magnetoresistance (MR) data have been symmetrized to eliminate possible contribution from the Hall resistance.

Angle resolved photoemission spectroscopy

The electronic band structure measurements were performed at High energy resolution spectrometer (HERS): Angle-resolved photoemission spectroscope (ARPES) at Advanced Light Source (ALS) beamline end station 10.0.1.1. The energy resolution was set to be better than 20 meV and the angular resolution was better than 0.2° for all the measurements [45]. The samples were mounted on copper sample holders, then posts were attached to their upper surface using silver epoxy. Then they were transferred to the high vacuum ARPES chamber and cleaved *in situ* at a pressure better than 10^{-10} torr and measurements were performed at a temperature of 18 K.

Theoretical calculations:

The *ab initio* calculations based on density functional theory (DFT) were performed using the projector augmented-wave (PAW) potentials [46] implemented in the Vienna Ab initio Simulation Package (VASP) code [47–49]. Calculations are made within the generalized

gradient approximation (GGA) in the Perdew, Burke, and Ernzerhof (PBE) parameterization [50]. The energy cutoff for the plane-wave expansion was set to 300 eV, while f electrons were treated as a core states. Optimizations of structural parameters (lattice constants and atomic positions) are performed in the primitive unit cell using the $15 \times 15 \times 7$ \mathbf{k} -point grid in the Monkhorst–Pack scheme [51]. As a break of the optimization loop, we take the condition with an energy difference of 10^{-6} eV and 10^{-8} eV for ionic and electronic degrees of freedom. The topological properties, as well as the electronic surface states, were studied using the tight binding model in the maximally localized Wannier orbitals basis [52, 53]. This model was constructed from exact DFT calculations in a primitive unit cell (containing one formula unit), with $10 \times 10 \times 6$ Γ -centered \mathbf{k} -point grid, using the WANNIER90 software [54]. During the calculations, the f electrons of Tb were treated as a core state. The electronic surface states were calculated using the surface Green’s function technique for a semi-infinite system [55], implemented in WANNIERTOOLS [56].

III. RESULTS AND DISCUSSION

Crystal and electronic structure

Similar to other $LnSbTe$ materials, $TbSbTe$ also crystallizes in the tetragonal $P4/nmm$ space group (No. 129) having the unit cell parameters $a = b = 4.25$ Å and $c = 9.212$ Å [44]. The atoms are located in the high symmetry Wyckoff positions with Tb at $2c : \frac{1}{4}, \frac{1}{4}, 0.2759$, Sb at $2a : \frac{3}{4}, \frac{1}{4}, 0$ and Te at $2c : \frac{1}{4}, \frac{1}{4}, 0.6244$ [43, 44, 57] (Laue X-ray diffraction pattern and energy-dispersive X-ray spectroscopy (EDX) spectrum are presented in supplementary material (SM)). The crystal structure of $TbSbTe$ presented in Fig. 1(a), comprises stacking of two Te-Tb-Te-Tb zigzag slabs having a $(\frac{1}{2}, \frac{1}{2}, z)$ shift relative to each other that sandwich each square-planar Sb net when viewed along the c axis [43](see SM).

The Brillouin zone (BZ) and its 2D projection onto the (001) plane is presented in SM. Fig. 1(b) displays the calculated bulk band structure with (blue bands) and without (yellow bands) the effect of SOC. The locations corresponding to the nodal points observed in the experimental findings are indicated with green boxes. The nodal points can be tracked along the k_z plane to the parallel HS directions to perceive their inclusion in a continuum of intersections. The bands of interest, taking part in formation of the nodal line features are marked with CB1, CB2, VB1 and VB2 in Fig. 1(b).

Bulk thermodynamic and electronic transport properties

The heat capacity data presented in Fig. 1(c) corroborates the AFM order in TbSbTe. The AFM phase transition manifests itself as a distinct λ type anomaly in $C(T)$, the position of which perfectly coincides with T_N determined from the magnetic data. Above about 100 K, $C(T)$ saturates at a value of 75.7 J/mol K) that is very close to the Dulong-Petit limit $3nR = 74.79$ J/mol K ($n = 3$ is the number of atoms per unit formula, and R stands for the gas constant). It should be noted that this finding notably differs from the results published before [44]. Here, it should also be emphasized that the quantitative analysis of $C(T)$ of TbSbTe, either within the framework of the simplified Debye model ($C \sim T^3$) or full Debye or Debye-Einstein formulas, is not possible without knowing the Schottky contribution from crystalline electric field excitations, which cannot be neglected at temperatures $T > 6$ K. In contrast, $C(T)$ in the AFM region is likely dominated by magnon contribution, which may be highly complex in nature, as suggested by the neutron diffraction results indicating the presence below T_N of several competing commensurate and incommensurate magnetic orderings [43].

Fig. 1(d) shows the temperature dependence of the magnetic susceptibility ($\chi \equiv M/H$) of TbSbTe measured in a magnetic field applied along the crystallographic c -axis. In agreement with the previous reports [43, 44], $\chi(T)$ shows a sharp maximum, marking the transition from PM to AFM state. The Néel temperature derived from this data is 5.1 K, that is lower than $T_N = 6.4$ K given in Ref. [43], yet fairly close to $T_N = 6.0$ K determined in Ref. [44]. As can be inferred from Fig. 1(d), in the PM state, $\chi(T)$ can be approximated by the modified Curie-Weiss (MCW) law, $\chi = \chi_o + \frac{C}{(T-\theta_p)}$, with the parameters $\chi_o = 6.4663 \times 10^{-6}$ emu/gOe, $C = 0.02635$ emu K/gOe and $\theta_p = -11.8749(3)$ K. The term χ_o is a sum of all the temperature independent contributions to the magnetic susceptibility due to conduction electrons, core electrons, and polarization effects. The effective magnetic moment μ_{eff} , calculated from the value of the Curie constant C , equals $9.28 \mu_B/\text{f.u.}$, which is very close to the theoretical prediction for free Tb^{+3} ion ($9.72 \mu_B$). The negative sign of the PM Curie temperature θ_p signals the predominance of AFM exchange interactions, in line with the AFM character of the electronic ground state in TbSbTe. It is worth noting that the values of μ_{eff} and θ_p somewhat differ from those given in Ref. [44] ($\mu_{eff} = 9.76$ and $\theta_p = -36$ K) for $H \parallel c$, which may signal some difference in the samples used in the two

studies (in Ref. [43], a polycrystal was measured so no direct comparison is justified in the case of a highly anisotropic material like TbSbTe).

The SM shows the magnetization $M(H)$ in TbSbTe measured at $T = 2$ K in external magnetic field confined in the crystallographic basal plane. In agreement with the results shown in Ref. [44], the isotherm exhibits three inflection points of metamagnetic-like character. Examining the derivative dM/dH vs. H (also shown in the SM) one finds the values of critical fields $H_1 = 19.4$ kOe, $H_2 = 39.8$ kOe and $H_3 = 46$ kOe which notably differ from those reported before ($H_1 = 10.5$ kOe, $H_2 = 20.8$ kOe and $H_3 = 38.2$ kOe) [44]. The occurrence of multi step changes in $M(H)$ can be associated with a complex non-collinear magnetic structure in zero magnetic field that at $T = 2$ K is defined by two propagation vectors $\mathbf{k}_1 = (\frac{1}{2} 0 0)$ and $\mathbf{k}_2 = (\frac{1}{2} 0 \frac{1}{4})$ [43]. It is known that multi-k spin structures are susceptible to external magnetic field which often results in multiple field-induced rearrangements. As can be inferred from the $M(H)$ isotherms (presented in the SM) measured in the PM state are featureless.

The temperature dependence of the electrical resistivity $\rho(T)$ measured within the tetragonal plane of TbSbTe is shown in Fig. 1(e). Both the magnitude and the shape of $\rho(T)$ reflect a semimetallic character of the compound. The $\rho(T)$ curve features a broad hump around 150 K, which may be associated to the interplay of gradual damping in charge carriers concentration and increase in scattering cross-section both occurring with decreasing temperature [43, 44, 58, 59]. Another feature in $\rho(T)$ is an upturn in the vicinity of T_N followed by a sharp peak near 5 K (see the inset to Fig. 1(e)) that manifests the onset of the ordered state. The prior study revealed a broad hump in $\rho(T)$ occurring around 240 K, however no clear anomaly at T_N was detected. The difference in the hump position may be attributed to diverse carrier concentrations in the crystals investigated. It seems likely that the same factor is responsible for the dissimilarities observed near T_N .

The transverse magnetoresistance (MR) = $[\rho(H)/\rho(0) - 1] \times 100$, of TbSbTe was measured with electric current flowing in the basal plane and magnetic field directed along the tetragonal c-axis at several temperatures below and above T_N (see Fig. 1 (f)). At 2 K, MR reaches in 9 T a value of 20%, which agrees with the previous study [44].

Observation of nodal line states

In order to reveal the electronic structure of the compound, the Fermi surface (FS) map along with its second derivative (SD), collected at 60 eV incident photon energy are presented

in the top panel of Figs. 2(a and b), respectively. As can be inferred from Fig. 2(c), the experimental ARPES data can be very well reproduced in the calculations based on the density functional theory (DFT) (presented in Figs. 2(h-k)). At the $k_x - k_y$ plane, the FS consists of two diamond shaped iso-centric (around Γ point) sheets. Examination of the constant energy contours (CECs) at higher binding energies (see Figs. 2(d-g)) below the Fermi level indicates convergence of the two-sheeted diamond-like structure into a singular sheet. This coalesced single sheet retains the single sheet character till 300 meV of binding energy. However, near 500~600 meV (see CECs measured at higher binding energy presented in SM, FS and CECs measured at different incident photon energies are also presented in the SM), the layers gradually diverge and reverts to its dual layer nature.

To better understand the band crossings in the band structure of TbSbTe, we looked into the ARPES dispersion maps along different HS directions ($\bar{\Gamma} - \bar{X}$, $\bar{\Gamma} - \bar{M}$ and $\bar{X} - \bar{M}$). The dispersion maps along $\bar{\Gamma} - \bar{X}$ and $\bar{X} - \bar{M}$, measured at an incident photon energy of 60 eV, are presented in Figs. 3(a) and (d) (dispersion maps at different HS directions measured at other incident photon energies are presented in SM). In Fig. 3(a), along $\bar{X} - \bar{\Gamma} - \bar{X}$, two distinct crossing points can be observed (marked with yellow arrow in 3(b)), which are parts of the nodal lines, a common feature for the isostructural $LnSbTe$ materials [34, 37, 40]. These features were reported in the recent theoretical studies on TbSbTe as well [44]. The first crossing occurs at the \bar{X} point which can be better observed in the SD plot of the dispersion map presented in Fig. 3(b) (also see the SM, which presents the dispersion map, its second derivative, and momentum dispersion curve at an incident photon energy of 50 eV to ascertain the presence of the Dirac like crossing).

The band crossing at X point remains robust against consideration of SOC as its protected by the additional nonsymmorphic symmetry, a well known phenomena in this system of materials. The experimentally obtained dispersion maps at different incident photon energies, parallel to $\Gamma - X$ (or $Z - R$) direction are presented in SM, which show the consistent presence of this crossing at the \bar{X} point at all photon energies, suggesting the crossing is a part of out of plane nodal line along k_z . The second crossing along the $\bar{\Gamma} - \bar{X}$ direction occurs approximately near 350 meV below the Fermi level. Theoretical calculations suggest existence of a small gap in the $k_z=0$ plane, which widens as we move towards the $k_z = \pi$ plane. However, this gap remained indiscernible in any of the dispersion cuts in different incident photon energies. Next, we move onto the $\bar{M} - \bar{X} - \bar{M}$ HS direction. Fig. 3(d),

presents the dispersion cut along $\bar{M} - \bar{X} - \bar{M}$, its second derivative and its theoretically calculated surface spectrum (Figs. 3(e) and (f)). An electron like pocket is present along this direction (dispersion map along $\bar{M} - \bar{X} - \bar{M}$ measured at other photon energies are presented in SM, which is characteristic of $LnSbTe$ type materials [31, 38, 42]. Bulk band calculations and surface projected spectrum, both exhibit similar pocket like feature suggesting presence of surface and bulk bands forming the pocket. Proceeding to the dispersion cut along the $\bar{M} - \bar{\Gamma} - \bar{M}$, presented in Fig. ??(a), two linear bands with different velocities converge to form an intersection, which is well reproduced in surface projected calculations presented at Fig. 4(c). This intersection near 200 meV, is a part of the nodal line which spans a whole $k_x - k_y$ plane surrounding the Γ point, this loop like feature is fairly evident from the CECs presented in Fig. 2 as well. Again, contrasting the experimental observations, bulk calculation (Fig. 1(b)) suggests that, a gap occurs at the intersection of bands CB2 and VB2 (see Fig. 1(b)), which persists in a reduced form, if SOC is taken into account. This gap was also beyond detection limits of the ARPES detector. Another notable aspect is a hole pocket like feature which can also be seen centering the Γ (or Z) point in cuts parallel to both $\Gamma - X$ and $\Gamma - M$ directions (see Figs. 3 and 4 respectively), throughout all the incident photon energies (presented in SM), but its spectral intensity was highly sensitive to the incident photon energy.

Thermodynamic, magnetic and transport measurements on $TbSbTe$ single crystals coherently exhibit the AFM to PM phase transition near 5.1 K. The electronic band structure of $TbSbTe$, in ARPES spectrographs, exhibit two isocentric diamond shaped sheets around the Γ point similar to other $LnSbTe$ and $ZrSiS$ type materials. For $TbSbTe$ the double-sheet is consistently present throughout the FS, unlike heavier members of $LnSbTe$ (for an example $HoSbTe$ [59]), where the bands tend to gap out while radially going towards the $\bar{\Gamma} - \bar{M}$ direction. Another feature of this FS is, the bands are not as well separated as in $NdSbTe$ [38] or $PrSbTe$ [42, 60], nor coalesced into a single sheet like $GdSbTe$ [31]. The nodal line features observed in the cuts parallel to the $\bar{\Gamma} - \bar{X}$ are well reproduced in bulk electronic calculations. In space group $P4/nmm$, symmetries in combination with nonsym-morphic symmetry plays a crucial role in realizing enforced degeneracy in the vicinity of Fermi energy. Dirac like crossings observed in the HS directions parallel to $\Gamma - X$ and $\Gamma - M$ (which are not located at exact HS points X or M) are protected by $C_{2\nu}$ symmetry, although consideration of SOC destabilizes these nodal crossings. Despite the theoretical predictions

of destabilized nodal line features along $\Gamma - X$ and $\Gamma - M$, in experimental observations, the nodal lines remain ungapped. This phenomenon could potentially be ascribed to constrained k_z resolution within the vacuum ultraviolet region, resulting in the energy cuts encompassing a spectrum of k_z values rather than being confined to a specific k_z value. An alternate explanation might stem from the prevalent incongruity between experimental results and theoretical predictions often observed in $4f$ systems. On the other hand, nonsymmorphic (glide) symmetry protects the out of plane crossing along k_z direction (along the $X - R$ HS direction)(See Fig. 1(b)), making TbSbTe a genuine nodal line semimetal candidate.

IV. CONCLUSION

To summarize, we present comprehensive temperature-dependent thermodynamic and electric transport investigations, which consistently indicates an AFM to PM transition at $T_N = 5.1$ K. Concurrently, we studied the electronic band structure of a new member of the $LnSbTe$ family, TbSbTe, using high-resolution ARPES combined with theoretical first-principles calculations. Our electronic structure study revealed multiple band intersections, including a Dirac like crossing along the $\Gamma - X$ HS direction, which is part of a nodal line extending along $X - R$ bulk direction. This crossing remains ungapped over k_z , as established in both our theoretical work considering the effect of SOC and our experimental ARPES-based observations. These results implicate TbSbTe as a promising candidate for examining the interaction of symmetry, topology and SOC in $LnSbTe$ series of materials.

ACKNOWLEDGEMENTS

M. N. acknowledges support from the National Science Foundation under the CAREER award DMR-1847962 and the Air Force Office of Scientific Research for MURI Grant No. FA9550-20-1-0322. D. K. and T.R. were supported by the National Science Centre (Poland) under research grant 2021/41/B/ST3/01141. V. B. and S. R. acknowledge the support from Idaho National Laboratory's Laboratory Directed Research and Development (LDRD) program under the Department of Energy (DOE) Idaho Operations Office Contract DEAC07-05ID14517. K. G. acknowledges support from the Division of Materials Science

and Engineering, Office of Basic Energy Sciences, Office of Science of the U. S. Department of Energy (U.S. DOE). A. P. acknowledges the support by National Science Centre (NCN, Poland) under Projects No. 2021/43/B/ST3/02166 and also appreciates the funding in the frame of scholarships of the Minister of Science and Higher Education (Poland) for outstanding young scientists (2019 edition, No. 818/STYP/14/2019). This research utilized resources of the ALS at the Lawrence Berkeley National Laboratory, which is a DOE Office of Science User Facility under Contract No. DE-AC02-05CH11231. Pressure-dependent magnetic measurements were performed at the State University of New York (SUNY), Buffalo State, and supported by the National Science Foundation, Launching Early-Career Academic Pathways in the Mathematical and Physical Sciences (LEAPS-MPS) program under Award No. DMR-2213412. We express our gratitude to Dr. Sung-Kwan Mo for providing valuable support with the beamline at the Advanced Light Source (ALS).

REFERENCES

- [1] M. Z. Hasan and C. L. Kane, Colloquium: Topological insulators. *Rev. Mod. Phys.* **82**, 3045–3067 (2010).
- [2] X.-L. Qi and S.-C. Zhang. Topological insulators and superconductors. *Rev. Mod. Phys.* **83**, 1057–1110 (2011).
- [3] M. Z. Hasan, S.-Y. Xu, and M. Neupane, Topological Insulators, topological Dirac semimetals, topological crystalline insulators, and topological Kondo insulators. In *Topological insulators: fundamentals and perspectives*, edited by Ortmann, Frank et al., 55-100 (John Wiley & Sons, United States, 2015).
- [4] M. Sato and Y. Ando, Topological superconductors: a review. *Rep. Prog. Phys.* **80**, 076501 (2017).
- [5] Z. Wang, Y. Sun, X.-Q. Chen, C. Franchini, G. Xu, H. Weng, X. Dai, and Z. Fang, Dirac semimetal and topological phase transitions in A_3Bi ($A = Na, K, Rb$). *Phys. Rev. B* **85**, 195320 (2012).
- [6] M. Neupane, S.-Y. Xu, R. Sankar, N. Alidoust, G. Bian, C. Liu, I. Belopolski, T.-R. Chang, H.-T. Jeng, H. Lin, A. Bansil, F. Chou, and M. Z. Hasan, Observation of a three-dimensional topological Dirac semimetal phase in high-mobility Cd_3As_2 . *Nat. Commun.* **5**, 3786 (2014).
- [7] Z. K. Liu, B. Zhou, Y. Zhang, Z. J. Wang, H. M. Weng, D. Prabhakaran, S.-K. Mo, Z. X. Shen,

- Z. Fang, X. Dai, Z. Hussain, and Y. L. Chen, Discovery of a three-dimensional topological Dirac semimetal Na_3Bi . *Science* **343**, 864-867 (2014).
- [8] B.-J. Yang and N. Nagaosa, Classification of stable three-dimensional Dirac semimetals with nontrivial topology. *Nat. Commun.* **5**, 1 (2014).
- [9] S.-Y. Xu, I. Belopolski, N. Alidoust, M. Neupane, G. Bian, C. Zhang, R. Sankar, G. Chang, Z. Yuan, C.-C. Lee, S.-M. Huang, H. Zheng, J. Ma, D. S. Sanchez, B. Wang, A. Bansil, F. Chou, P. P. Shibayev, H. Lin, S. Jia, and M. Z. Hasan, Discovery of a Weyl fermion semimetal and topological Fermi arcs. *Science* **349**, 613-617 (2015).
- [10] B. Q. Lv, H. M. Weng, B. B. Fu, X. P. Wang, H. Miao, J. Ma, P. Richard, X. C. Huang, L. X. Zhao, G. F. Chen, Z. Fang, X. Dai, T. Qian, and H. Ding, Experimental discovery of Weyl Semimetal TaAs. *Phys. Rev. X* **5**, 031013 (2015).
- [11] A. A. Soluyanov, D. Gresch, Z. Wang, Q. Wu, M. Troyer, X. Dai, and B. A. Bernevig, Type-II Weyl semimetals. *Nature* **527**, 495-498 (2015).
- [12] B. Yan and C. Felser, Topological materials: Weyl semimetals. *Annu. Rev. Condens. Matter Phys.* **8**, 337-354 (2017).
- [13] A. P. Sakhya, C.-Y. Huang, G. Dhakal, X.-J. Gao, S. Regmi, B. Wang, W. Wen, R.-H. He, X. Yao, R. Smith, M. Sprague, S. Gao, B. Singh, H. Lin, S.-Y. Xu, F. Tafti, A. Bansil, and M. Neupane, Observation of Fermi arcs and Weyl nodes in a noncentrosymmetric magnetic Weyl semimetal. *Phys. Rev. Mater.* **7**, L051202 (2023).
- [14] C. Fang, Y. Chen, H.-Y. Kee, and L. Fu, Topological nodal line semimetals with and without spin-orbital coupling. *Phys. Rev. B* **92**, 081201 (2015).
- [15] Q.-F. Liang, J. Zhou, R. Yu, Z. Wang, and H. Weng, Node-surface and node-line fermions from nonsymmorphic lattice symmetries. *Phys. Rev. B* **93**, 085427 (2016).
- [16] M. Neupane, I. Belopolski, M. M. Hosen, D. S. Sanchez, R. Sankar, M. Szlawska, S.-Y. Xu, K. Dimitri, N. Dhakal, P. Maldonado, P. M. Oppeneer, D. Kaczorowski, F. Chou, M. Z. Hasan, and T. Durakiewicz, Observation of topological nodal fermion semimetal phase in ZrSiS . *Phys. Rev. B* **93**, 201104 (2016).
- [17] L. M. Schoop, M. N. Ali, C. Straßer, A. Topp, A. Varykhalov, D. Marchenko, V. Duppel, S. S. Parkin, B. V. Lotsch, and C. R. Ast, Dirac cone protected by non-symmorphic symmetry and three-dimensional Dirac line node in ZrSiS . *Nat. Commun.* **7**, 11696 (2016).
- [18] G. Bian, T.-R. Chang, R. Sankar, S.-Y. Xu, H. Zheng, T. Neupert, C.-K. Chiu, S.-M. Huang,

- G. Chang, I. Belopolski, Topological nodal-line fermions in spin-orbit metal PbTaSe₂. *Nat. Commun.* **7**, 10556 (2016).
- [19] M. M. Hosen, K. Dimitri, I. Belopolski, P. Maldonado, R. Sankar, N. Dhakal, G. Dhakal, T. Cole, P. M. Oppeneer, D. Kaczorowski, F. Chou, M. Z. Hasan, T. Durakiewicz, and M. Neupane, Tunability of the topological nodal-line semimetal phase in ZrSiX-type materials ($X = \text{S, Se, Te}$). *Phys. Rev. B* **95**, 161101 (2017).
- [20] S. Li, Y. Liu, B. Fu, Z.-M. Yu, S. A. Yang, and Y. Yao, Almost ideal nodal-loop semimetal in monoclinic CuTeO₃ material. *Phys. Rev. B* **97**, 245148 (2018).
- [21] N. P. Armitage, E. J. Mele, and A. Vishwanath, A. Weyl and Dirac semimetals in three-dimensional solids. *Rev. Mod. Phys.* **90**, 015001 (2018).
- [22] J. Zhan, J. Li, W. Shi, X.-Q. Chen, and Y. Sun, Coexistence of Weyl semimetal and Weyl nodal loop semimetal phases in a collinear antiferromagnet. *Phys. Rev. B* **107**, 224402 (2023).
- [23] Y. Wu, L.-L. Wang, E. Mun, D. D. Johnson, D. Mou, L. Huang, Y. Lee, S. L. Bud'ko, P. C. Canfield, and A. Kaminski, Dirac node arcs in PtSn₄. *Nat. Phys.* **12**, 667-671 (2016).
- [24] G. Dhakal, F. Kabir, A. K. Nandy, A. Aperis, A. P. Sakhya, S. Pradhan, K. Dimitri, C. Sims, S. Regmi, M. M. Hosen, Y. Liu, L. Persaud, D. Kaczorowski, P. M. Oppeneer, and M. Neupane, Observation of anisotropic Dirac cones in the topological material Ti₂Te₂P. *Phys. Rev. B* **106**, 125124 (2022).
- [25] C.-K. Chiu and A. P. Schnyder, Classification of reflection-symmetry-protected topological semimetals and nodal superconductors. *Phys. Rev. B* **90**, 205136 (2014).
- [26] B.-J. Yang, T. A. Bojesen, T. Morimoto, and A. Furusaki, Topological semimetals protected by off-centered symmetries in nonsymmorphic crystals. *Phys. Rev. B* **95**, 075135 (2017).
- [27] Y. X. Zhao and A. P. Schnyder, Nonsymmorphic symmetry-required band crossings in topological semimetals. *Phys. Rev. B* **94**, 195109 (2016).
- [28] B. J. Wieder and C. L. Kane, Spin-orbit semimetals in the layer groups. *Phys. Rev. B* **94**, 155108 (2016).
- [29] L. M. Schoop, A. Topp, J. Lippmann, F. Orlandi, L. M"uchler, M. G. Vergniory, Y. Sun, A. W. Rost, V. Duppel, M. Krivenkov, S. Sheoran, P. Manuel, A. Varykhalov, B. Yan, R. K. Kremer, C. R. Ast, and B. V. Lotsch, Tunable Weyl and Dirac states in the nonsymmorphic compound CeSbTe. *Sci. Adv.* **4**, eaar2317 (2018).
- [30] A. A. Burkov, M. D. Hook, and L. Balents, Topological nodal semimetals. *Phys. Rev. B* **84**,

- 235126 (2011).
- [31] M. M. Hosen, G. Dhakal, K. Dimitri, P. Maldonado, A. Aperis, F. Kabir, C. Sims, P. Riseborough, P. M. Oppeneer, D. Kaczorowski, and M. Neupane, Discovery of topological nodal-line fermionic phase in a magnetic material GdSbTe. *Sci. Rep.* **8**, 31296 (2018).
- [32] M. Yang, Y. Qian, D. Yan, Y. Li, Y. Song, Z. Wang, C. Yi, H. L. Feng, H. Weng, and Y. Shi, Magnetic and electronic properties of a topological nodal line semimetal candidate: HoSbTe. *Phys. Rev. Mater.* **4**, 094203 (2020).
- [33] N. Shumiya, J.-X. Yin, G. Chang, M. Yang, S. Mardanya, T.-R. Chang, H. Lin, M. S. Hossain, Y.-X. Jiang, T. A. Cochran, Q. Zhang, X. P. Yang, Y. Shi, and M. Z. Hasan, Evidence for electronic signature of a magnetic transition in the topological magnet HoSbTe *Phys. Rev. B* **106**, 035151 (2022).
- [34] B. Lv, J. Chen, L. Qiao, J. Ma, X. Yang, M. Li, M. Wang, Q. Tao, and Z.-A. Xu, Magnetic and transport properties of low-carrier-density Kondo semimetal CeSbTe. *J. Phys. Condens. Matter* **31**, 355601 (2019).
- [35] P. Li, B. Lv, Y. Fang, W. Guo, Z. Wu, Y. Wu, D. Shen, Y. Nie, L. Petaccia, C. Cao, Z.-A. Xu, and Y. Liu, Charge density wave and weak Kondo effect in a Dirac semimetal CeSbTe. *Sci. China Phys. Mech. & Astron.* **64**, 237412 (2021).
- [36] L. Y. Cao, M. Yang, L. Wang, Y. Li, B. X. Gao, L. Wang, J. L. Liu, A. F. Fang, Y. G. Shi, and R. Y. Chen, Optical study of the topological materials $LnSbTe$ ($Ln = La, Ce, Sm, Gd$). *Phys. Rev. B* **106**, 245145 (2022).
- [37] Y. Wang, Y. Qian, M. Yang, H. Chen, C. Li, Z. Tan, Y. Cai, W. Zhao, S. Gao, Y. Feng, S. Kumar, E. F. Schwier, L. Zhao, H. Weng, Y. Shi, G. Wang, Y. Song, Y. Huang, K. Shimada, Z. Xu, X. J. Zhou, and G. Liu, Spectroscopic evidence for the realization of a genuine topological nodal-line semimetal in LaSbTe. *Phys. Rev. B* **103**, 125131 (2021).
- [38] S. Regmi, R. Smith, A. P. Sakhya, M. Sprague, M. I. Mondal, I. B. Elius, N. Valadez, A. Ptok, D. Kaczorowski, and M. Neupane, Observation of gapless nodal-line states in NdSbTe. *Phys. Rev. Mater.* **7**, 044202 (2023).
- [39] K. Pandey, R. Basnet, A. Wegner, G. Acharya, M. R. U. Nabi, J. Liu, J. Wang, Y. K. Takahashi, B. Da, and J. Hu, Electronic and magnetic properties of the topological semimetal candidate NdSbTe. *Phys. Rev. B* **101**, 235161 (2020).
- [40] S. Regmi, G. Dhakal, F. C. Kabeer, N. Harrison, F. Kabir, A. P. Sakhya, K. Gofryk, D. Kac-

- zorowski, P. M. Oppeneer, and M. Neupane, Observation of multiple nodal lines in SmSbTe. *Phys. Rev. Mater.* **6**, L031201 (2022).
- [41] K. Pandey, D. Mondal, J. W. Villanova, J. Roll, R. Basnet, A. Wegner, G. Acharya, M. R. U. Nabi, B. Ghosh, J. Fujii, J. Wang, B. Da, A. Agarwal, I. Vobornik, A. Politano, S. Barraza-Lopez, and J. Hu, Magnetic topological semimetal phase with electronic correlation enhancement in SmSbTe. *Adv. Quantum Technol.* **4**, 2100063 (2021).
- [42] S. Regmi, I. B. Elius, A. P. Sakhya, M. Sprague, M. I. Mondal, N. Valadez, V. Buturlim, K. Booth, T. Romanova, K. Gofryk, A. Ptok, D. Kaczorowski, and M. Neupane, Electronic structure in a rare-earth based nodal-line semimetal candidate PrSbTe. *Phys. Rev. Mater.* **8**, L041201 (2024).
- [43] I. Plokhikh, V. Pomjakushin, D. J. Gawryluk, O. Zaharko, and E. Pomjakushina, Competing magnetic phases in LnSbTe (Ln = Ho and Tb) *Inorg. Chem.* **61**, 11399-11409 (2022).
- [44] F. Gao, J. Huang, W. Ren, H. Wu, M. An, X. Wu, L. Zhang, T. Yang, A. Wang, Y. Chai, X. Zhao, T. Yang, B. Li, and Z. Zhang, magnetic and magnetotransport properties of the magnetic topological nodal-line semimetal TbSbTe. *Adv. Quantum Technol.*, 2200163 (2023).
- [45] M. Neupane, M. M. Hosen, I. Belopolski, N. Wakeham, K. Dimitri, N. Dhakal, J.-X. Zhu, M. Z. Hasan, E. D. Bauer, and F. Ronning, Observation of Dirac-like semi-metallic phase in NdSb. *J. Phys. Condens. Matter* **28**, 23LT02 (2016).
- [46] P. E Blöchl, Projector augmented-wave method. *Phys. Rev. B* **50**, 17953 (1994).
- [47] G. Kresse, J. and Hafner, Ab initio molecular-dynamics simulation of the liquid-metal–amorphous-semiconductor transition in germanium. *Phys. Rev. B* **49**, 14251 (1994).
- [48] G. Kresse, and J. Furthmüller, Efficient iterative schemes for ab initio total-energy calculations using a plane-wave basis set. *Phys. Rev. B* **54**, 11169 (1996).
- [49] G. Kresse, and D. Joubert, From ultrasoft pseudopotentials to the projector augmented-wave method. *Phys. Rev. B* **59**, 1758 (1999).
- [50] John P. Perdew, Kieron Burke, and Matthias Ernzerhof. Generalized Gradient Approximation Made Simple. *Phys. Rev. Lett.* **77**, 3865-3868 (1996).
- [51] H. J. Monkhorst, and J. D. Pack, Special points for Brillouin-zone integrations. *Phys. Rev. B* **13**, 5188 (1976).
- [52] N. Marzari, and D. Vanderbilt, Maximally localized generalized Wannier functions for composite energy bands. *Phys. Rev. B* **56**, 12847 (1997).

- [53] I. Souza, N. Marzari, and D. Vanderbilt, Maximally localized Wannier functions for entangled energy bands. *Phys. Rev. B* **65**, 035109 (2001).
- [54] G. Pizzi, V. Vitale, R. Arita, S. Blügel, F. Freimuth, G. Géranton, M. Gibertini, D. Gresch, C. Johnson, T. Koretsune, J. Ibáñez-Azpiroz, H. Lee, J.-M. Lihm, D. Marchand, A. Marrazzo, Y. Mokrousov, J. I. Mustafa, Y. Nohara, Y. Nomura, L. Paulatto, S. Poncé, T. Ponweiser, J. Qiao, F. Thöle, S. S. Tsirkin, M. Wierzbowska, N. Marzari, D. Vanderbilt, I. Souza, A. A. Mostofi, and J. R. Yates, WANNIER90 as a community code: new features and applications. *J. Phys.: Condens. Matter* **32**, 165902 (2020).
- [55] M. P. L. Sancho, J.M. Lopez Sancho, J. M. L. Sancho, and J. Rubio, Highly convergent schemes for the calculation of bulk and surface Green functions. *J. Phys. F: Met. Phys.* **15**, 851 (1985).
- [56] Q. S. Wu, S. N. Zhang, H. -F. Song, M. Troyer, and A. A. Soluyanov, WANNIERTOOLS: An open-source software package for novel topological materials. *Comput. Phys. Commun.* **224**, 405 (2018).
- [57] I. Plokhikh, V. Pomjakushin, D. Jakub Gawryluk, O. Zaharko, and E. Pomjakushina, On the magnetic structures of 1:1:1 stoichiometric topological phases LnSbTe (Ln= Pr, Nd, Dy and Er). *J. Magn. Magn. Mater.* **583**, 171009 (2023).
- [58] P. Gebauer, H. Poddig, L. T. Corredor-Bohorquez, T. V. Menshchikova, I. P. Rusinov, P. Golub, F. Caglieris, C. Benndorf, T. Lindemann, E. V. Chulkov, A. U. B. Wolter, B. Büchner, T. Doert, and A. Isaeva, Heavy-atom antiferromagnet GdBiTe: an interplay of magnetism and topology in a symmetry-protected topological semimetal. *Chem. Mater.* **33**, 2420-2435 (2021).
- [59] S. Yue, Y. Qian, M. Yang, D. Geng, C. Yi, S. Kumar, K. Shimada, P. Cheng, L. Chen, Z. Wang, H. Weng, Y. Shi, K. Wu, and B. Feng, Topological electronic structure in the antiferromagnet HoSbTe. *Phys. Rev. B* **102**, 155109 (2020).
- [60] D. Yuan, D. Huang, X. Ma, X. Chen, H. Ren, Y. Zhang, W. Feng, X. Zhu, B. Wang, X. He, J. Wu, S. Tan, Q. Hao, Q. Zhang, Y. Liu, Q. Liu, Z. Liu, C. Cao, Q. Chen, and X. Lai, Observation of Dirac nodal line states in topological semimetal candidate PrSbTe. *Phys. Rev. B* **109**, 045113 (2024).

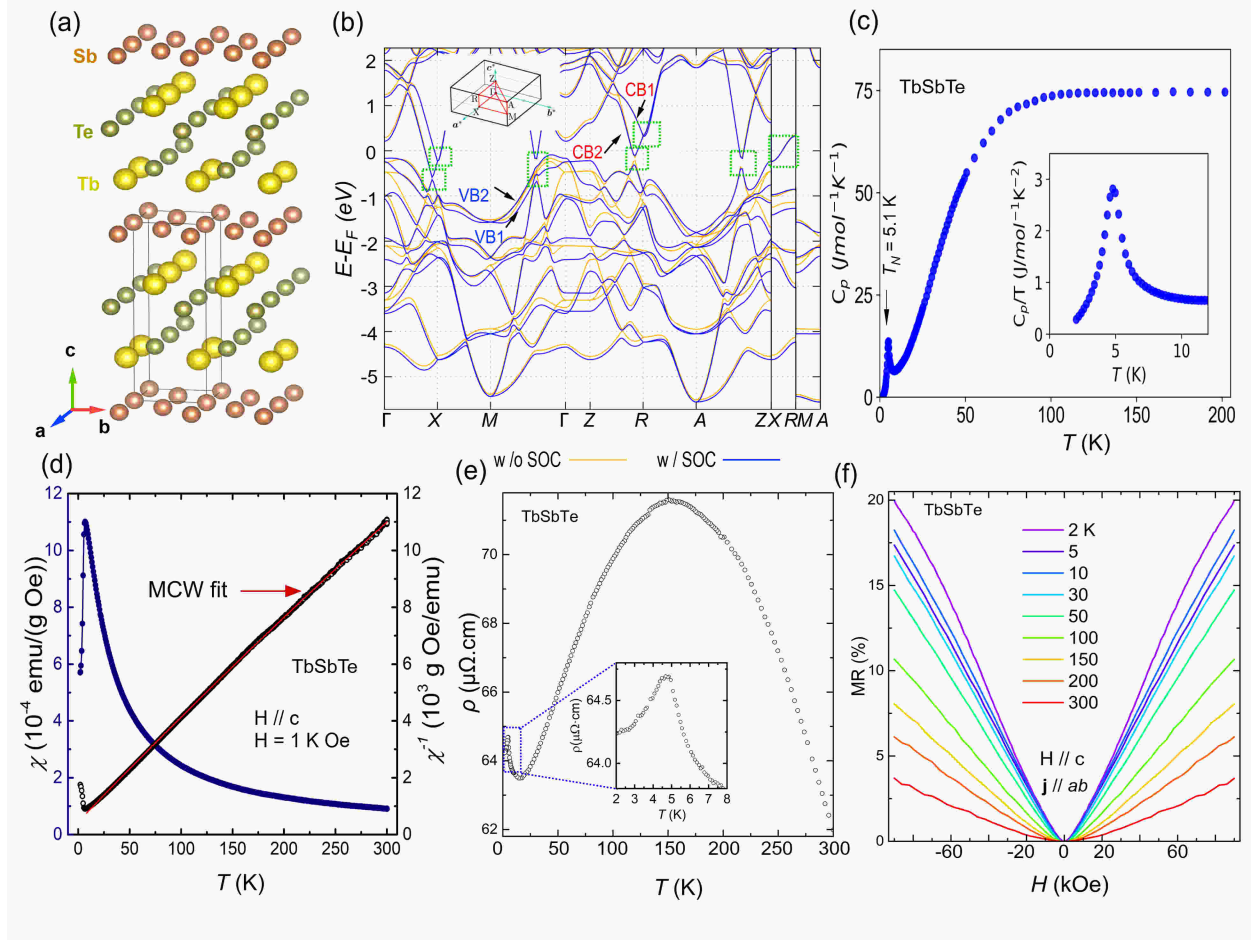


FIGURE 1. Crystal structure, electronic band structure, thermodynamic, magnetic and transport properties of TbSbTe. (a) Crystal structure of TbSbTe, two zig-zag chains of Tb-Te are sandwiched by square planar 2D Sb-nets. (b) Calculated band structure without considering SOC (yellow) and with consideration of SOC (blue), the positions of the nodal lines (which corresponds to the experimental observations) are marked with green boxes. (c) Temperature dependence of specific heat of TbSbTe, the black arrow indicates the AFM to PM phase transition, C_p/T vs T curve zoomed in at the low temperature range is presented in the inset. (d) Temperature dependent dc-susceptibility χ and χ^{-1} , measured in 1 kOe. The red line indicates a fit using the modified Curie-Weiss law. (e) Temperature dependence of electrical transport (inset: a magnified view at low temperature range showing AFM to PM transition). (f) Magnetic field dependent magnetoresistance (MR) isotherms ranging from 2 K to 300 K.

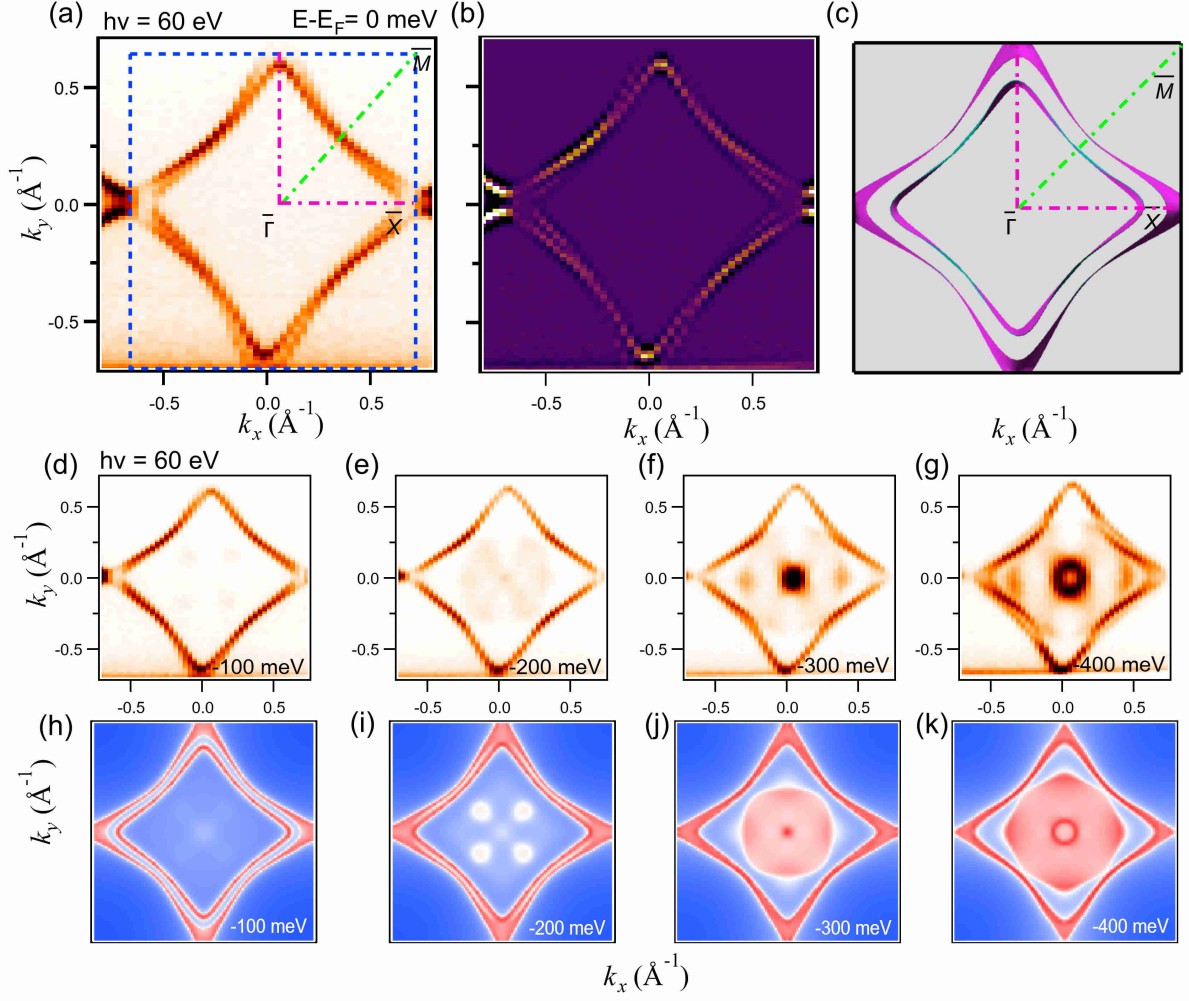


FIGURE 2. Fermi surface and Constant energy contour maps of TbSbTe. (a) Experimentally observed Fermi surface map of TbSbTe at an incident photon energy of 60 eV, the surface Brillouin zone is marked with a blue-dashed square and all the HS points ($\bar{\Gamma}$, \bar{M} and \bar{X}) are marked. (b) Second derivative (SD) of the experimental Fermi surface. (c) Fermi surface obtained from DFT based calculations with the inclusion of SOC. (d-g) Experimentally observed constant energy contour maps at 100 meV, 200 meV, 300 meV and 400 meV below the Fermi surface, (h-k) theoretically calculated constant energy contours, with their binding energies marked on each of the contour plots. The ARPES measurements were done at Advanced Light Source (ALS) beamline 10.0.1.1 at a temperature of 18 K.

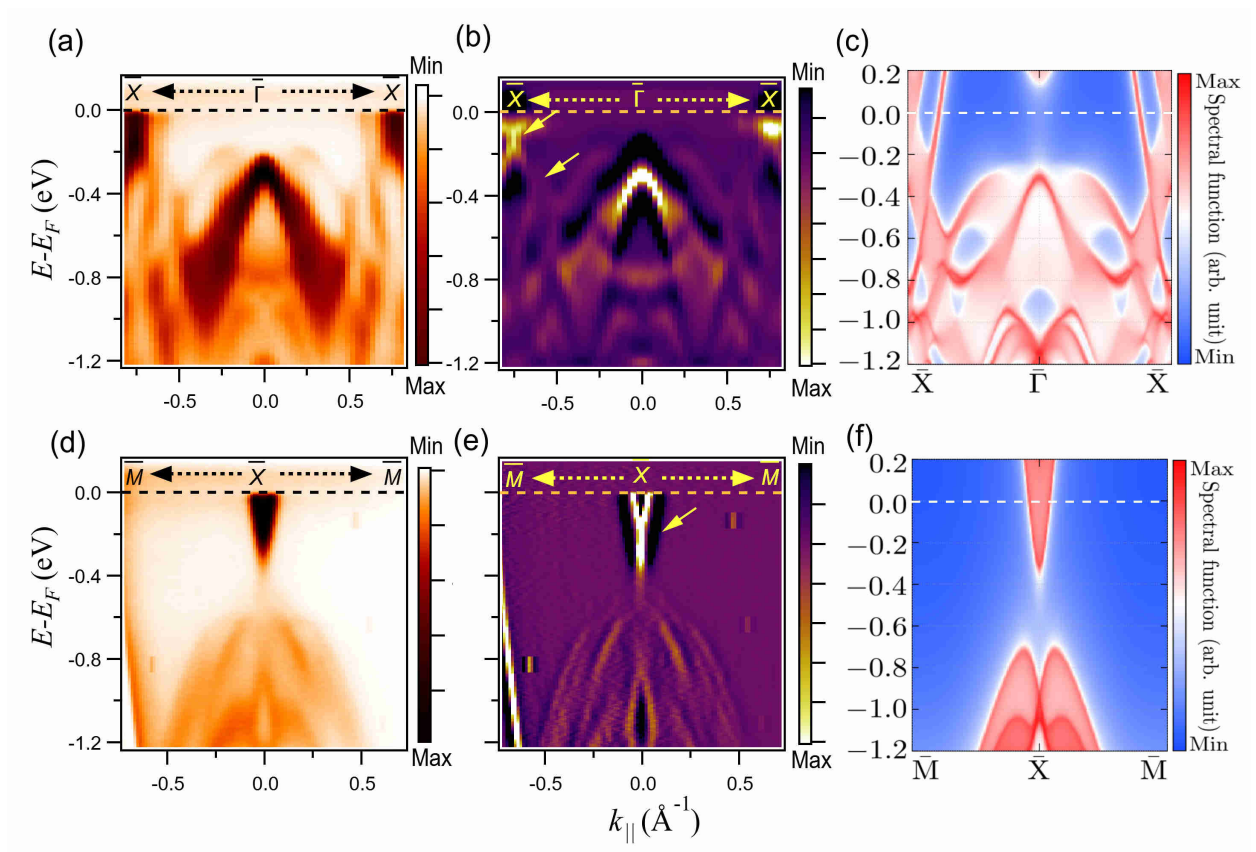


FIGURE 3. Observation of nodal line features parallel to the $\bar{X}-\bar{\Gamma}-\bar{X}$ and $\bar{M}-\bar{X}-\bar{M}$ directions. (a) Electronic dispersion map along $\bar{X}-\bar{\Gamma}-\bar{X}$ direction, (b) second derivative of the dispersion map along $\bar{X}-\bar{\Gamma}-\bar{X}$, the nodal points which are parts of nodal lines are marked with yellow arrows. (c) the theoretically calculated surface projected band structure along $\bar{X}-\bar{\Gamma}-\bar{X}$. (d) dispersion maps along $\bar{M}-\bar{X}-\bar{M}$, (e) their second derivative and (f) theoretically calculated surface projected band structure. All the ARPES dispersion maps were collected at beam line 10.0.1.1 in Advanced Light Source (ALS) at a temperature of 18 K.

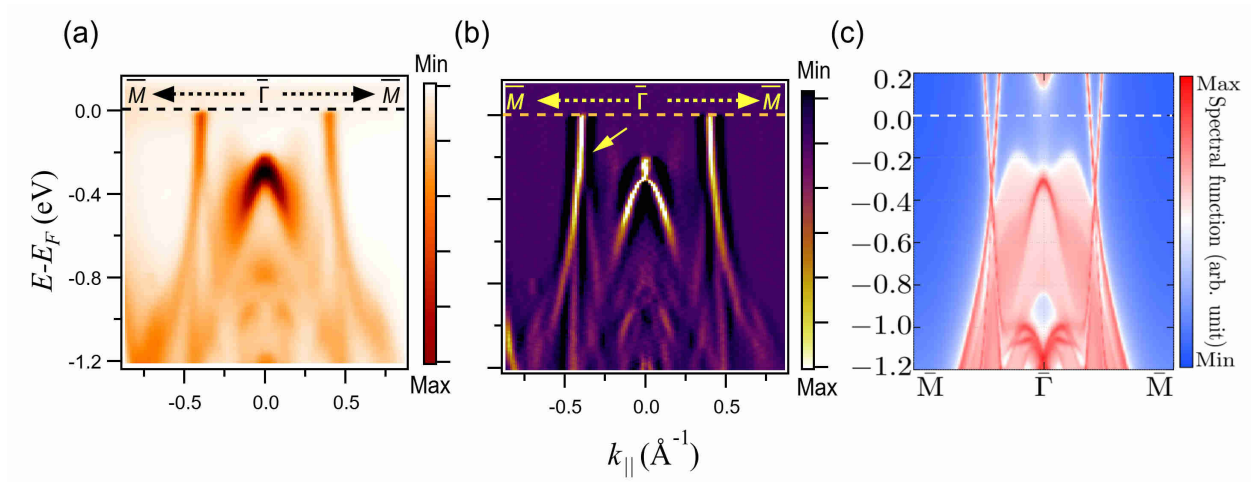


FIGURE 4. Observation of nodal states at the $\bar{M} - \bar{\Gamma} - \bar{M}$ direction. (a) Dispersion map along $\bar{M} - \bar{\Gamma} - \bar{M}$ HS direction measured with 60 eV incident photon energy at a temperature of 25 K at ALS beamline 10.0.1.1. (b) Second derivative of $\bar{M} - \bar{\Gamma} - \bar{M}$ dispersion map, and (c) theoretically calculated surface band map along $\bar{M} - \bar{\Gamma} - \bar{M}$.